



HAL
open science

Gas temperature measurements from ps-TALIF in highly collisional plasmas

Abdoulaye Constant Siby, Dimitrios Stefas, Yanis Agha, Laurent Invernizzi, Kristaq Gazeli, Guillaume Lombardi, Khaled Hassouni, Swaminathan Prasanna

► **To cite this version:**

Abdoulaye Constant Siby, Dimitrios Stefas, Yanis Agha, Laurent Invernizzi, Kristaq Gazeli, et al.. Gas temperature measurements from ps-TALIF in highly collisional plasmas. *Physics of Plasmas*, 2024, 31 (3), pp.3506. 10.1063/5.0189326 . hal-04202967v2

HAL Id: hal-04202967

<https://hal.science/hal-04202967v2>

Submitted on 26 Mar 2024

HAL is a multi-disciplinary open access archive for the deposit and dissemination of scientific research documents, whether they are published or not. The documents may come from teaching and research institutions in France or abroad, or from public or private research centers.

L'archive ouverte pluridisciplinaire **HAL**, est destinée au dépôt et à la diffusion de documents scientifiques de niveau recherche, publiés ou non, émanant des établissements d'enseignement et de recherche français ou étrangers, des laboratoires publics ou privés.

This is the author's peer reviewed, accepted manuscript. However, the online version of record will be different from this version once it has been copyedited and typeset.

PLEASE CITE THIS ARTICLE AS DOI: 10.1063/1.50189326

17 I. INTRODUCTION

18 Gas temperature (T_g) is one of the most important fundamental properties whose ac-
19 curate measurement is challenging in strongly non-equilibrium reactive plasmas. Different
20 non-invasive optical methods based on rovibrationally resolved emission spectroscopy, light
21 scattering techniques [1], Coherent anti-Stokes Raman spectroscopy (CARS) [2] etc. have
22 been used to measure T_g .

23 The most prominent philosophy relies on measurement of the rotational temperature from
24 the emission spectra of molecular rovibrational bands [3], laser absorption and fluorescence[4]
25 or Raman scattering [2, 5]. Evidently these methods rely on the assumption of equilibrium
26 between translational and rotational temperatures which is not necessarily satisfied for all
27 discharge conditions. The other approach of measuring gas temperatures refers to the use
28 of the Doppler width of atoms where high resolution spectra of atomic lines from emission,
29 absorption or laser induced fluorescence are recorded. Unfortunately, these methods can
30 be employed only for elevated gas temperatures and the lightest element (H-atom). The
31 limitation of the different approaches is that they require application of multiple paral-
32 lel diagnostics to converge towards the “real” gas temperature while development of new
33 techniques continues to attract active interest. Emission based methods are most commonly
34 used to probe the emissive regions of the plasma while absorption based methods are used to
35 record absorption lines of interest. Both methods rely on performing line-of-sight integrated
36 measurements. Contrary to these two methods, measurements based on laser scattering and
37 fluorescence achieve better space-time resolution in sub-millimeter and picosecond space-
38 and time-scales respectively [6], and can also be used to probe non-emissive regions of the
39 plasma.

40 This paper explores a straightforward and direct approach to determine the gas temper-
41 ature in collisional plasmas from picosecond Two Photon Absorption Laser Induced Flu-
42 orescence (ps-TALIF). TALIF has become the standard approach to measure atom densities
43 in reactive environments [6]. The principle of TALIF is to excite ground-state atoms to a
44 fluorescing state by absorption of two photons of a pulsed laser and subsequently record-
45 ing the resulting fluorescence signal. Rapid advancement in the development of lasers with
46 picosecond (ps) and femtosecond pulse width as well as acquisition systems such as streak
47 cameras having ps-time resolution has extended the application of TALIF for diagnosing

This is the author's peer reviewed, accepted manuscript. However, the online version of record will be different from this version once it has been copyedited and typeset.

PLEASE CITE THIS ARTICLE AS DOI: 10.1063/1.50189326

48 reactive moderate to high pressure plasmas where the effective lifetimes τ_X of the laser-
 49 excited atoms are of sub-nanosecond or even ps-time scales[6]. Indeed, τ_X serves as a probe
 50 of local plasma conditions as it encapsulates all the radiative and collisional quenching pro-
 51 cesses [7, 8]. In particular, the collisional quenching is directly related to the temperature
 52 of the gas and therefore τ_X provides direct access to the gas temperature. It has to be
 53 noted that gas temperatures can also be determined through the measurement of Doppler
 54 broadening of fluorescence line[9] by TALIF. However, the large laser broadening character-
 55 istic of most commercial pulsed lasers that is necessary for measurements of atom densities
 56 in such reactive conditions restricts their straightforward extension towards gas tempera-
 57 ture measurements. Most importantly, this new approach enjoys all major advantages of a
 58 typical TALIF-based diagnostics such as probing non-emissive post-discharge regions with
 59 sub-millimeter space and ps-time resolutions.

60 We will demonstrate this novel approach using a MW microplasma source operating with
 61 pure hydrogen under moderate pressure conditions ranging between 50 to 125 mbar. The
 62 present paper is organized as follows: the experimental setup used for the present study is
 63 described in section II, section III describes the theoretical principle of atom density and
 64 gas temperature measurements using ps-TALIF and Optical emission spectroscopy (OES),
 65 results and discussion are presented in section IV and finally the important conclusions are
 66 summarized in section V.

67 II. EXPERIMENTAL SETUP

68 An in-house developed MW plasma microtorch based on coaxial transmission line res-
 69 onator (CLTR) was used for the present work[11]. This torch has been used to produce
 70 carbon nanostructures such as nanodiamonds from gases H_2/CH_4 and Ar at moderate pres-
 71 sure ranges (20 to 150 mbar). The scope of this study is restricted to pure hydrogen plasmas.
 72 The plasma is generated in a small gap of 500 μm between the central metallic core and the
 73 coaxial ground. The flow rate of H_2 gas was set at 100 sccm for all the experiments, while
 74 the pressure in the chamber was regulated using a pressure regulator (a solenoid normally
 75 closed valve of 1000 sccm flow capacity at the downstream) at a prescribed value between
 76 50 and 100 mbar with a fluctuation of ± 1 mbar .

77 The experimental setup used for the laser diagnostics in the present study is depicted

This is the author's peer reviewed, accepted manuscript. However, the online version of record will be different from this version once it has been copyedited and typeset.

PLEASE CITE THIS ARTICLE AS DOI: 10.1063/1.50189326

78 in Figure 1 showing the ps-laser, streak camera and the reactor chamber housing the MW
 79 plasma source. Detailed description of ps-laser and streak camera has been provided in
 80 [6, 12]. In brief, the ps-laser system can generate pulses up to $60 \mu J$ /pulse with a pulse
 81 width of around 10 ps at a repetition frequency of 5 Hz at 205.03 nm (the two-photon
 82 excitation wavelength of H-atom). A fused-silica lens with a focal length 500 mm was used
 83 to obtain a laser spot size with diameter of $500 \mu m$ at the center of the plasma chamber. The
 84 energy of the laser beam exiting the plasma chamber is measured by means of a calorimeter
 85 (Coherent J-10MB-LE) connected to a digital oscilloscope. The energy of the laser was
 86 controlled using the internal amplification of the laser system and a combination of neutral
 87 density filters. The fluorescence signal was collected in the perpendicular direction to the
 88 laser beam using an achromatic lens of 100 mm focal length and an appropriate band-pass
 89 filter mounted in front of the entrance slit of the streak camera. The microplasma torch was
 90 embedded into an octagonal vacuum chamber with three optical view-ports dedicated for
 91 laser diagnostics. The UV-laser beam enters the chamber through a first UV-transparent
 92 fused silica window, crosses the reactive flow generated by the plasma where it induces
 93 two-photon excitation of the hydrogen atoms produced by dissociation and then exits the
 94 chamber through the second fused-silica window. The resulting fluorescence was collected
 95 in the perpendicular direction to the laser beam through a borosilicate window. The reactor
 96 chamber was placed on a translation stage that allowed moving the plasma perpendicularly
 97 to the laser beam, cf. Figure 1, so as to investigate the radial variation of the atom density
 98 and plasma temperature. The path of the laser was aligned with the x axis of the reactor
 99 with focus close to the axis of the microplasma. Calibration of the z-axis was performed
 100 accurately using the laser calorimeter and streak camera to identify the measurable region
 101 where both the laser and the fluorescence are not blocked by the surface of the plasma. The
 102 plasma source was displaced with respect to the laser until the laser signal remains constant
 103 on both the calorimeter and the streak camera. This position was found to be 0.5 mm below
 104 the electrode surface and has been marked as the origin 0 for all future representations.

105 Optical emission spectroscopy (OES) (cf. Figure 2) has been performed independently
 106 using a spectrometer having focal length of 1m (Jobin Yvon THR 1000) equipped with a
 107 1200 grooves per mm grating that is blazed at 500 nm and a photomultiplier tube. The
 108 microplasma torch was placed on the longer arm of a KF-40 Tee with a borosilicate optical
 109 window on the opposite. The KF-40 tee was placed on a x-y linear stage so that the center

This is the author's peer reviewed, accepted manuscript. However, the online version of record will be different from this version once it has been copyedited and typeset.

PLEASE CITE THIS ARTICLE AS DOI: 10.1063/1.50189326

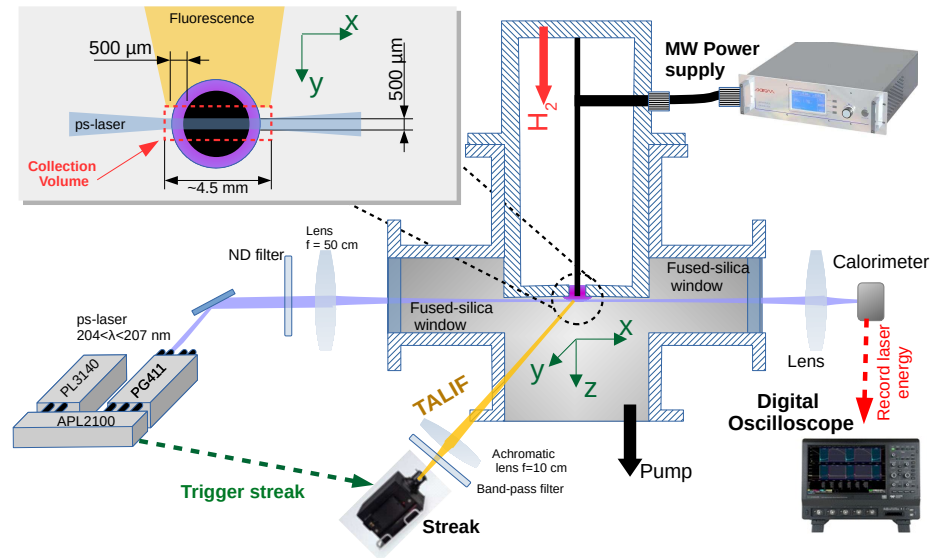


FIG. 1. Schematic of the experimental setup for TALIF showing the MW plasma reactor, ps-laser and streak camera

110 of the microplasma was aligned with the vertical slit (1 cm height and 40 μm width) of the
 111 spectrometer. 2f-arrangement was used to collect the emission signal where a bi-convex lens
 112 of 100 mm focal length was placed in between the plasma and the slit of the spectrometer
 113 at equal distance of 200 cm. This arrangement ensures that the emission from the entire
 114 radial section of the microplasma to be captured by the spectrometer and coupled with a
 115 photomultiplier tube measures the section averaged-local plasma quantities deduced from
 116 the emission spectra such as rotational temperature and H-atom density .

117 Actually, the radial sections traced by the laser overlaps with that of the signal from
 118 emission. However, the volumes traced by the laser and the emissive volume captured by the
 119 spectrometer are not exactly the same. Nevertheless, as the first point of laser measurement
 120 is within 500 μm from the surface of the torch, the line-averaged TALIF measurements from
 121 this position can be compared with the average quantities measured by OES and therefore
 122 will be used to validate the methodology proposed in this study.

This is the author's peer reviewed, accepted manuscript. However, the online version of record will be different from this version once it has been copyedited and typeset.

PLEASE CITE THIS ARTICLE AS DOI: 10.1063/1.50189326

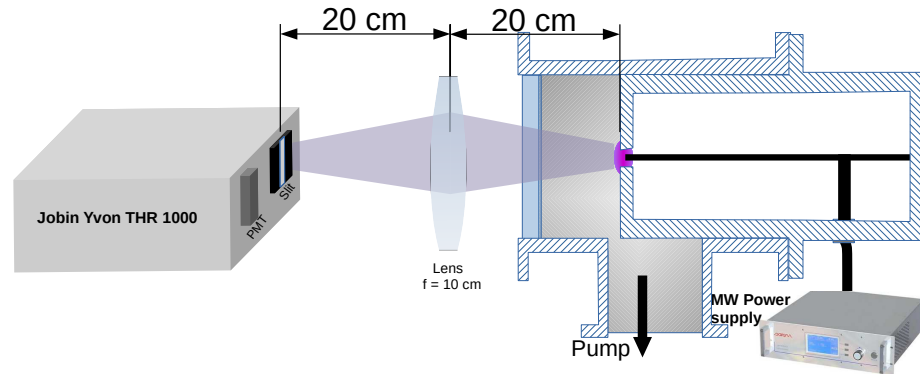


FIG. 2. Schematic of the experimental setup for performing OES.

123 III. METHODOLOGY

124 A. Measurement of atom densities

125 The general principle of TALIF is discussed in [6]. The absolute density of atomic species
126 i measured using TALIF can be written as

$$n_i = n_C \frac{\int_t \int_\lambda S_{F_i} \eta_C T_C \sigma_C A_C \tau_C E_C^2 \lambda_C^2}{\int_t \int_\lambda S_{F_C} \eta_i T_i \sigma_i A_i \tau_i E_i^2 \lambda_i^2} \quad (1)$$

127 with subscript i and C referring to the reactive and calibrating atomic species respectively,
128 n_i is the density of the reactive species i , $\int_t \int_\lambda S_{F_i}$ is the temporally and spectrally integrated
129 fluorescence signal, η_i/η_C and T_i/T_C are the quantum efficiency of the detector and trans-
130 mission of the optics at the fluorescence wavelength respectively, σ_i/σ_C is the two-photon
131 excitation cross-section, A_i/A_C is the Einstein coefficient of the radiative decay of the laser
132 excited state and τ_i/τ_C is the experimentally measured fluorescence decay time of the laser
133 excited state, E_i/E_C and λ_i/λ_C are the energy and wavelength of the laser used for making
134 the TALIF measurements. For performing ps-TALIF on H-atom, the H-atom ground-state
135 is excited to the H($n=3$) by absorption of two photons at an excitation wavelength of 205.08
136 nm and the resulting fluorescence is collected from the Balmer α line ($H_{n=3} \rightarrow H_{n=2}$) at
137 656.3 nm.

138 In equation 1, quantities $\int_t \int_\lambda S_{F_i}$ and τ_i are directly measurable from ps-TALIF signals
139 captured using a streak camera. The streak images are treated according to the procedure

This is the author's peer reviewed, accepted manuscript. However, the online version of record will be different from this version once it has been copyedited and typeset.

PLEASE CITE THIS ARTICLE AS DOI: 10.1063/1.50189326

140 discussed in Invernizzi et al. [12, 13] to obtain temporally integrated fluorescence signal
 141 $\int_t S_{F_i,\lambda}$ and τ_i at a laser excitation wavelength λ . Subsequently, $\int_t \int_\lambda S_{F_i}$ is determined by
 142 integrating the temporal fluorescence signals over several spectral points around the two
 143 photon peak excitation wavelength. The shape of the spectral fluorescence signal, also re-
 144 ferred to as overlap integral $g(\delta\lambda_C)$, is the convolution of line-widths of laser and broadened
 145 line-widths of the excited species. The ps-laser is characterized by a large laser line-width
 146 when compared to the the Doppler line widths of H-atom (<3 pm) in the range of tem-
 147 perature considered in this study. As a result, the overlap integral $g(\delta\lambda_C)$ is dominated by
 148 the laser line width and was found to be 30 ± 2 pm measured over different operating con-
 149 ditions (pressure and MW power). This allows for application of peak-excitation method
 150 (PEM) [10] that allows for measurement of $\int_t \int_\lambda S_{F_i}$ directly from a single temporal inte-
 151 grated fluorescence signal at the two photon laser excitation wavelength $\int_t S_{F_i,\lambda_i}$ as the two
 152 quantities are related through the relation $\int_t \int_\lambda S_{F_i}; g(\delta\lambda_C) = \int_t S_{F_i,\lambda_i}$ and the atom densities
 153 are determined as follows

$$n_i = n_C \frac{\int_t S_{F_i,\lambda_i} g(\delta\lambda_C) \eta_C T_C \sigma_C A_C \tau_C E_C^2 \lambda_C^2}{\int_t S_{F_C,\lambda_C} g(\delta\lambda_i) \eta_i T_i \sigma_i A_i \tau_i E_i^2 \lambda_i^2} \quad (2)$$

154 Such simplification allows for greatly reducing the acquisition time for one data point when
 155 compared to full acquisition of the absorption line profile and has been used for the present
 156 study.

157 Following Invernizzi et al. [12], the time window of the streak image was ideally set
 158 to 5 ns in order to accurately extract the τ_H over the range of experimental conditions
 159 considered in this work. Actually, the raw TALIF signal captured using a streak camera is
 160 a 2D image where x-axis (673 pixels) and the y-axis (508 pixels) are indicative of the spatial
 161 (i.e. x-axis of the reactor) and the temporal dimension respectively. The slit of the streak
 162 camera is horizontal (i.e. along x-axis) and captures a zone of fluorescence of about 4.5 ± 2
 163 mm centered around the axis of the plasma torch as shown in Figure 3. The large focal
 164 length of the laser focussing lens (500 mm) ensures that the laser cross-section ($\sim 500\mu m$)
 165 remains constant throughout the fluorescence zone. The height of the plasma with respect
 166 to the laser (i.e. in the z direction) was varied in order to construct the 2D fields of H-atom
 167 density and other associated quantities in the x-z plane.

168 To perform absolute density measurements, the H-atom density calibration was per-
 169 formed using krypton [14]. For this purpose, ps-TALIF measurements were performed in

This is the author's peer reviewed, accepted manuscript. However, the online version of record will be different from this version once it has been copyedited and typeset.

PLEASE CITE THIS ARTICLE AS DOI: 10.1063/1.50189326

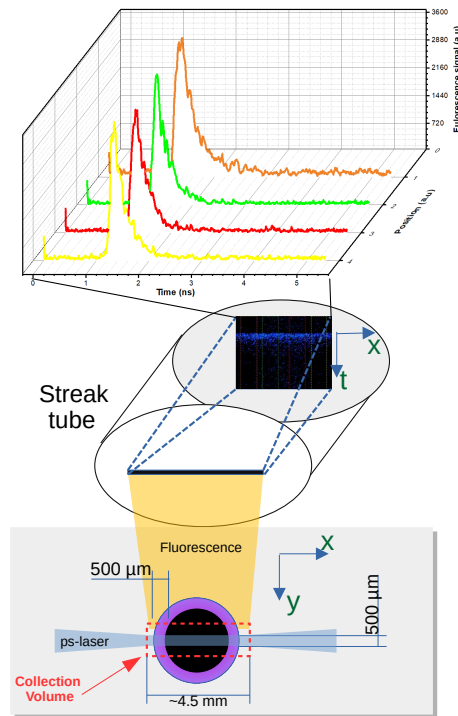


FIG. 3. Illustration of the fluorescence captured by the streak camera.

170 pure Krypton in a quartz cuvette at 200 Pa. However, as the optical parameters such as
 171 transmittance of cuvette and the plasma reactor are different, we determined their ratio
 172 from the ratio of H-atom densities obtained using ps-TALIF and actinometry. In actinom-
 173 etry, H-atom densities are determined from the ratios of line intensities of H_{α} and Argon
 174 lines at 750.4 nm[15] of a H_2 plasma with < 1% of argon. This ratio was found to be 0.78 at
 175 a reference condition (pressure 100 mbar and 90 W power). This condition actually corre-
 176 sponds to the formation of diamond nanoparticles with a gas mixture of H_2 - CH_4 [11]. This
 177 value was used for all subsequent measurements.

178 **B. Gas temperature measurements**

179 The effective lifetime τ_i characterizes the collisional and radiative decay processes of the
180 excited species following the laser excitation and can be written as:

$$\frac{1}{\tau_i} = A_i + Q_i = A_i + \frac{P}{k_B T_g} \sum_j^{\text{quenchants}} k_{Q_{i/j}} x_j \quad (3)$$

181 Where Q_i and A_i are the quenching rate and the total Einstein coefficient of radiative decay
182 of the excited state. P is the local pressure, T_g is the gas temperature, k_B is the Boltzmann
183 constant, and x_j is the molar fraction of the quenchant j . $k_{Q_{i/j}}$ is the rate coefficient of
184 quenching of excited species i by quenchant j and can be expressed as :

$$k_{Q_{i/j}} = \sigma_{Q_{i/j}} \nu_{i/j} = \sigma_{Q_{i/j}} \sqrt{\frac{8k_B T_g}{\pi \mu_{i/j}}} \quad (4)$$

185 where $\sigma_{Q_{i/j}}$ is the collisional quenching cross section, $\nu_{i/j}$ and $\mu_{i/j}$ are the mean thermal
186 velocity and the reduced mass of collision pair i/j .

187 The measurement of τ_i and exploitation of equation 3 allows one to gain more insight
188 about the reactive environment. For example, one can determine radiative decay rate $1/A_i$
189 and collisional quenching cross-section $\sigma_{Q_{i/j}}$ using the Stern-Volmer plot of $\frac{1}{\tau_i}$ over a range
190 of pressures covering three distinct regimes:

- 191
- Radiation dominated regime at extremely low pressures i.e. $A_i \gg Q_i$
 - Collision dominated regime at high pressures where $A_i \ll Q_i$
 - Competition between radiative and collisional processes at intermediate pressures i.e.
194 $A_i \sim Q_i$

195 Similarly, with the knowledge of radiative and collisional decay constants, it would be
196 possible to deduce the gas temperature T_g by rewriting equation 3 as

$$T_g = \frac{8}{\pi k_B} \left(\frac{P \tau_i}{1 - \tau_i A_i} \sum_j \frac{x_j \sigma_{Q_{i/j}}}{\sqrt{\mu_{i/j}}} \right)^2 \quad (5)$$

197 However, it is necessary to check the conditions of validity for estimating T_g from τ_i using
198 equation 5. The most important condition that needs to be accounted for is the collisionality
199 of the plasma $\gamma_i = 1 - \tau_i A_i$ which occupies the denominator of equation 5. It is easy to

This is the author's peer reviewed, accepted manuscript. However, the online version of record will be different from this version once it has been copyedited and typeset.

PLEASE CITE THIS ARTICLE AS DOI: 10.1063/1.50189326

200 notice that γ_i varies between 0 and 1 where the lower asymptotic limit $\gamma_i \rightarrow 0$ is indicative
 201 of radiation dominated decay process while the opposite $\gamma_i \rightarrow 1$ is indicative of collisional
 202 dominated regime. It is obvious that the retrieval of temperature is not applicable for
 203 radiative dominated decay regimes (mathematically as $\gamma_i \rightarrow 0, T_g \rightarrow \infty$). Moreover, the
 204 uncertainty analysis (cf. Appendix A) indicates that the propagation of errors is minimum
 205 when $\gamma \rightarrow 1$. For example, the errors emerging from different components can be amplified
 206 up to two folds when $\gamma_i = 0.5$ (see equation A3). Such collisional conditions would ensure
 207 thermal equilibrium of heavy species [16] which is key to the validity of equation 5. In
 208 fact, this is a huge advantage when compared to methods that depend on interpreting gas
 209 temperature from rovibrational molecular bands as one requires to check for the existence
 210 of equilibrium between rotational and translational modes as will be seen in the following
 211 paragraphs.

212 Gas temperatures have also been estimated using OES from the rotational temperatures
 213 of H_2 . For H_2 molecule, the most commonly used rotational bands are (i) R branch of the
 214 transition $G^1 \Sigma_g, \nu' = 0 \rightarrow B^1 \Sigma_u^+, \nu'' = 0$ and (ii) the Q-Branch $d^3 \Pi_u^-, \nu' = 0 \rightarrow a^3 \Sigma_g^+,$
 215 $\nu'' = 0$ of the Fulcher- α band[17–20]. For a rotational band under equilibrium, the rotational
 216 temperature can be determined using a Boltzmann plot. Though the rotational bands of H_2
 217 are spectrally distinct, the determination of gas temperature from the rotational temper-
 218 ature is not easy. The equivalence of rotational temperatures to gas kinetic temperatures
 219 broadly follow two distinct collisional regimes. Firstly, in a low collisional regime that occurs
 220 at low pressure, the excited states are populated due to the electron driven excitation of the
 221 ground state and therefore the rotational distribution of the emission lines are in fact a map
 222 of that of the ground state. On the other asymptotique end, when the collisional frequency
 223 is high enough to thermalize the excited state before photon emission, the rotational tem-
 224 peratures determined from the rotational constants of the excited states are reflective of the
 225 gas temperatures.

226 With respect to $d^3 \Pi_u^-$ of the Fulcher band in the the current experimental conditions,
 227 the collisional quenching time (~ 50 ns at 1000 K and 100 mbar) is of the same order of
 228 magnitude as that of its radiative decay (60 ns)[11]. Therefore, $d^3 \Pi_u^-$ undergo collisions and
 229 the rotational distribution of the excited states would not depict the ground state. However
 230 the number of collisions are not sufficient enough for the $d^3 \Pi_u^-$ to equilibriate with the gas
 231 temperature[11]. Therefore, the gas kinetic temperature would be between the upper and

This is the author's peer reviewed, accepted manuscript. However, the online version of record will be different from this version once it has been copyedited and typeset.

PLEASE CITE THIS ARTICLE AS DOI: 10.1063/1.50189326

232 lower limits of the rotational temperature determined from the rotational constants of the
 233 upper state $d^3 \Pi_u^-$ and the ground state $X^1\Sigma_g^+$.

234 On the other hand, the analysis of emission of $G^1 \Sigma_g \rightarrow B^1 \Sigma_u^+$ is much more complicated
 235 and remains poorly understood. The radiative decay and quenching times of the excited
 236 state $G^1 \Sigma_g$ are about 33 and 0.4 ns (1000 K and 100 mbar) respectively. This would mean
 237 that the decay of $G^1 \Sigma_g$ is dominated by quenching processes rather than the radiative decay.
 238 However, the T-R energy transfer is quite weak for H_2 and the small lifetimes makes ther-
 239 malization of $G^1 \Sigma_g$ improbable. This would mean that the rotational structure of $G^1 \Sigma_g$
 240 is filled by electron excitation of the ground state and therefore effectively map the ground
 241 state $X^1\Sigma_g^+$. However, contrary to the above stated hypothesis, several studies show that the
 242 G-band rotational temperature can be thermalized at moderate pressures (>20 mbar) and
 243 the rotational temperatures of $G^1 \Sigma_g$ can be reflective of the gas temperatures[18, 21–23].
 244 This observation is probably caused by the perturbations of $G^1 \Sigma_g$ by the vibrational states
 245 of $K^1\Sigma_g^+$ and inadequate understanding of mechanisms of de-excitation and energy relax-
 246 ation. In spite of the above limitations, rotational temperatures measured using Fulcher i.e.
 247 ($T_{rot}(d)$ and $T_{rot}(X)$) and G-band ($T_{rot}(G)$) will be used as a gauge for the gas temperatures
 248 measurements deduced from the TALIF.

249 IV. RESULTS AND DISCUSSION

250 The quadratic dependence of the fluorescence intensity with respect to the laser energy
 251 (as required by Equation 1) was verified for different operating conditions of H and Kr and
 252 is shown in Figure 4. Figure 5 compares the H-atom densities measured using ps-TALIF
 253 and actinometry. The two measurements are in relative agreement with each other in the
 254 ranges of pressure and power studied and validates the approach for absolute calibration
 255 used in the present study.

256 For the conditions examined in this paper, the plasma is highly collisional with τ_H rang-
 257 ing between 100 and 450 ps while $\gamma_H > 0.95$ (calculated using $A_{H(n=3)} = 4.41 \times 10^7 \text{ s}^{-1}$
 258 for Balmer α line[24]) as shown in Figure 6. The τ_H decreases with increase in pressure,
 259 indicating increase in collisionality. Therefore, in principle, one single fluorescence signal
 260 should be sufficient to simultaneously measure the H-atom density and T_g . This is evident
 261 from the positive correlation shared between τ_H and MW absorbed power and therefore T_g .

This is the author's peer reviewed, accepted manuscript. However, the online version of record will be different from this version once it has been copyedited and typeset.

PLEASE CITE THIS ARTICLE AS DOI: 10.1063/1.50189326

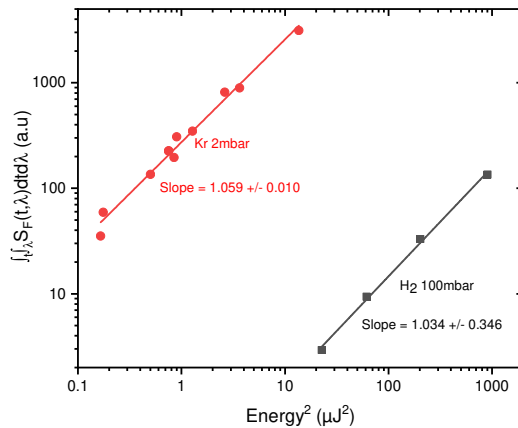


FIG. 4. Variations of S_{F_i} as a function of laser energy for H and Kr.

262 However, determination of τ_H with good accuracy is absolutely necessary for reliable
 263 retrieval of T_g . Invernizzi et al.[12] discuss the challenges of accurately extracting τ_i from
 264 raw ps-TALIF signals captured with a streak camera by taking into account the instrumental
 265 function of the detector, which must be removed from the raw ps-TALIF signal. Moving
 266 point averaging with a window size of 200 pixels (which covers approximately 1.5 mm) was
 267 performed to suppress the noise in the raw images and to obtain the average spatial variation
 268 of the derived fields such as H-atom densities and gas temperatures. The uncertainty of τ_i
 269 would naturally depend on the density of the probed atomic species. Lower atom densities
 270 would indicate lower TALIF signal intensity as well as increased noise, which would make
 271 it difficult to accurately extract τ_i from the raw TALIF data, hence including a larger
 272 uncertainty. Uncertainty on τ_H [12] was estimated within 5 % in our conditions, which
 273 makes the measurements of T_g by the approach discussed here fairly reasonable. The high-
 274 collisionality would mean that complex radiative processes that are associated to the $H(n =$
 275 $3)$ level have little influence while collisional processes dictate the values of τ_H . Therefore,
 276 as evident from equation 5, the knowledge of all collisional quenchers and corresponding
 277 composition and cross-section is necessary. H_2 is the main quencher with $\sigma_{H/H_2} = 98 \pm 10 \text{ \AA}^2$
 278 [8] while H-atom is a weak quencher with a much smaller $\sigma_{H/H}$ of 3.8 \AA^2 [25].

This is the author's peer reviewed, accepted manuscript. However, the online version of record will be different from this version once it has been copyedited and typeset.

PLEASE CITE THIS ARTICLE AS DOI: 10.1063/1.50189326

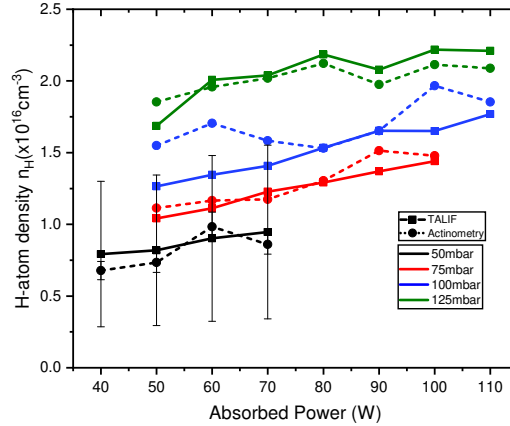


FIG. 5. H-atom densities measured using actinometry and ps-TALIF as a function of pressure and power.

279 The gas temperatures obtained from τ_H that represent the emissive region of the plasma
 280 has been compared with rotational temperature determined from the emission spectra of H₂
 281 rotational bands of R branch of the transition $G^1 \Sigma_g^+, \nu' = 0 \rightarrow B^1 \Sigma_u^+, \nu'' = 0$ and upper
 282 and lower temperature limits deduced from rotational temperature of the Q-Branch $d^3 \Pi_u,$
 283 $\nu' = 0 \rightarrow a^3 \Sigma_g^+, \nu'' = 0$ of the Fulcher- α band. The gas temperatures from τ_H compares
 284 well with $T_{rot}(G)$ and is about 300 K lower than that of the upper temperature limit of
 285 Fulcher i.e. $T_{rot}(d)$ at 100mbar. The comparison between $T_{rot}(G)$ and T_g from τ_H compare
 286 well within $\pm 25\%$ margin for the entire range of pressure and power studied as shown in
 287 Figure 7(b). Likewise, the comparison between $T_{rot}(d)$ and T_g from τ_H is within $\pm 25\%$,
 288 albeit with higher scatter than the former case as seen in Figure 7(c). Moreover, the Pearson
 289 correlation coefficient between $T_{rot}(G)$ and T_g is much better (~ 0.80) that that of $T_{rot}(d)$
 290 and T_g (~ 0.60). This is also indicative of the fact that $T_{rot}(G)$ is a better representative of
 291 T_g than that of $T_{rot}(d)$ for the ranges of pressure and power considered in this study.

292 Analysis of propagation of errors, (as explained in Appendix A, equation A1), indicates
 293 that the major contribution comes from the uncertainty of the collisional quenching cross-
 294 section σ_{H/H_2} for all the studied conditions as shown in Figure 8. Due to low dissociation ($<$

This is the author's peer reviewed, accepted manuscript. However, the online version of record will be different from this version once it has been copyedited and typeset.

PLEASE CITE THIS ARTICLE AS DOI: 10.1063/1.50189326

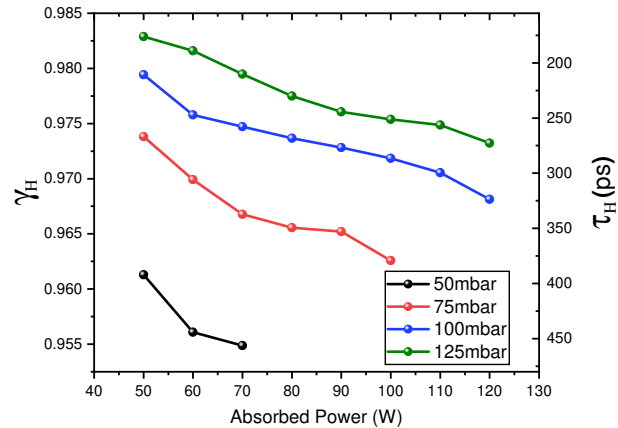


FIG. 6. Variation of τ_H extracted from ps-TALIF signals and corresponding γ_H as a function of pressure and power for the experimental conditions considered in this paper.

295 5%) as well as weak quenching by H-atoms ($\sigma_{H/H} \ll \sigma_{H/H_2}$), H-atom density does not play
 296 a major role towards the temperature measurements. For our experiments, the pressure was
 297 well controlled within ± 1 mbar or $\pm 2\%$ and therefore does not impact the overall uncertainty
 298 to a large extent. Therefore the only experimentally measured parameter that affects the
 299 temperature measurement is τ_H . Nevertheless, its contribution towards total uncertainty
 300 is low for most conditions with a maximum of 30% far away from the plasma zone where
 301 the temperature is much lower and close to ambient. However, due to the high uncertainty
 302 of σ_{H/H_2} of 10%, the minimum uncertainty of T_g translates to about 20% and marks the
 303 limitation of the present methodology. Therefore, an appropriate choice of collisional cross-
 304 sections is necessary for accurate measurement of gas temperature. For illustration, we have
 305 shown in Figure 7(a) the gas temperatures determined using the other values of σ_{H/H_2} cited
 306 in the literature, namely 65 [26, 27] and 156 [28] \AA^2 . The gas temperatures estimated using
 307 the respective σ_{H/H_2} are either too low or high when compared to the lower and upper limits
 308 of the rotational temperature determined from Fulcher to be realistic.

309 Moreover, we have used the cross-sections available in the literature and most of these
 310 cross-sections are constants. However, it is possible that these cross-sections indeed are de-

This is the author's peer reviewed, accepted manuscript. However, the online version of record will be different from this version once it has been copyedited and typeset.

PLEASE CITE THIS ARTICLE AS DOI: 10.1063/1.50189326

311 pendent on gas temperature and that would also have an impact on the final gas temperature
 312 retrieval. Having said that, the methodology proposed does not make any approximation
 313 on the dependence of gas-temperature on quench cross-sections and can easily incorpo-
 314 rate better cross-sections to further improve the accuracy. On the otherhand, the present
 315 approach can also be exploited as a tool to measure the temperature dependent collisional
 316 cross-sections when coupled with reliable gas temperature measurements from another com-
 317 plementary approach.

318 The differences between the measurements of gas temperature from τ_H and rotational
 319 temperatures from G-band are partly due to the spatial variation of gas temperatures which
 320 is actually captured in the raw fluorescence images while the emission spectra captures the
 321 entire emissive volume. Figure 9 shows the 2D contour plot of H-atom density and gas
 322 temperature at different pressure conditions and are consistent with the characteristics of
 323 the discharge with pressure. Both H-atom and T_g are much more homogeneous axially at
 324 lower pressures such as 50 and 75 mbar. However, as the thermal diffusion decreases with
 325 higher pressures, one can clearly recognize two hot local zones separated by a cold zone close
 326 to $z = 0$ plane indicative of the annular shape of the microplasma. One can clearly observe
 327 that there is a strong dissociation of H-atoms locally in these hot zones at 125 mbar which
 328 are absent at lower pressures. This is representative of the plasma-MW coupling where the
 329 volume of MW power deposition decreases with pressure. These spatial variation of both H-
 330 atom and T_g could not be visually deciphered from the raw fluorescence signals and could be
 331 only deduced from the post-treatment of these signals. More importantly, the method was
 332 able to capture the strong temperature gradients that are present in the present microplasma.
 333 The temperature differences between the hot-zones and surrounding regions were as high as
 334 600 K. Also, there is a sharp decrease in temperature and H-atom density away from the
 335 plasma discharge which are homogeneous within 3 mm from the plasma region. T_g becomes
 336 closer to ambient temperature within about 5 mm from the discharge zone. However, there
 337 is still a substantial amount of H-atom ($1 \times 10^{15} \text{ cm}^{-3}$) at such low temperatures which may
 338 be interesting for different applications such as elaboration or treatment of thermo-sensitive
 339 materials and carbon nanostructures such as nanodiamonds [11].

340 **V. CONCLUSION**

341 This work demonstrates a straightforward and reliable determination of gas tempera-
 342 tures from τ_H for highly collisional conditions. The advances in using ultrafast lasers and
 343 acquisition systems allows for much more access to the local plasma conditions prevailing
 344 in a complex reactive flow. The extension of the present methodology to complex gas mix-
 345 tures may be possible with careful considerations of different possible quenchers and their
 346 respective collisional cross-sections. The merit of this method lies in the fact that both
 347 atom-densities as well as gas temperatures can be obtained simultaneously from a single flu-
 348 orescence signal. Moreover, the method provides direct access to the gas kinetic temperature
 349 unlike methods that rely on the equilibrium of rovibrational distributions with gas temper-
 350 ature. Furthermore, unlike the Doppler broadening method[9] which requires obtaining the
 351 full spectral profile of the fluorescence line, gas temperatures can be deduced directly from
 352 one fluorescence decay signal obtained at the peak of the two-photon excitation[10]. As the
 353 measurements are spatially local, 2D (or even 3D) cartography of gas temperature can be
 354 constructed even in non-emissive regions of the reactive flow.

355 **ACKNOWLEDGEMENTS**

356 This work was funded by the French Agence Nationale de la Recherche (ANR), under
 357 grants ANR-22-CE51-0013 (project NANODIAPLAS) and ANR-22-CE51-0027-02 (project
 358 ULTRAMAP), Labex SEAM (ANR-10-LABX-0096; ANR-18-IDEX0001) and IDF regional
 359 project SESAME DIAGPLAS. One of the authors (Khaled Hassouni) acknowledges the
 360 support of the Institut Universitaire de France.

361 **Appendix A: Uncertainty analysis for gas temperature measurements**

362 The uncertainty of the gas temperature measurements ΔT_g is determined from the indi-
 363 vidual uncertainties of all the independent variables as follows:

$$\Delta T_g = \sqrt{\left(\frac{\partial T_g}{\partial P} \Delta P\right)^2 + \left(\frac{\partial T_g}{\partial A_i} \Delta A_i\right)^2 + \left(\frac{\partial T_g}{\partial \tau_i} \Delta \tau_i\right)^2 + \sum_j \left\{ \left(\frac{\partial T_g}{\partial \sigma_j} \Delta \sigma_j\right)^2 + \left(\frac{\partial T_g}{\partial x_j} \Delta x_j\right)^2 \right\}} \quad (\text{A1})$$

This is the author's peer reviewed, accepted manuscript. However, the online version of record will be different from this version once it has been copyedited and typeset.

PLEASE CITE THIS ARTICLE AS DOI: 10.1063/5.0189326

364 where the partial derivative of T_g with respect to the different independent variables are
 365 given by

$$\begin{aligned} \frac{\partial T_g}{\partial P} &= T_g \frac{2}{P} & \frac{\partial T_g}{\partial A_i} &= T_g \frac{2\tau_i}{\gamma_i} & \frac{\partial T_g}{\partial \tau_i} &= T_g \frac{2}{\gamma_i \tau_i} \\ \frac{\partial T_g}{\partial \sigma_j} &= \frac{16\sigma_j}{\pi k_B} \left(\frac{P\tau_i}{\gamma_i} \frac{x_j}{\sqrt{\mu_j}} \right)^2 & \frac{\partial T_g}{\partial x_j} &= \frac{16x_j}{\pi k_B} \left(\frac{P\tau_i}{\gamma_i} \frac{\sigma_j}{\sqrt{\mu_j}} \right)^2 \end{aligned} \quad (\text{A2})$$

366 In conditions where the degree of dissociation is small, and only one quencher species j is
 367 dominant (as seen in our experimental conditions), the uncertainty ΔT_g depends only on
 368 the relative uncertainty of individual variables as given below

$$\frac{\Delta T_g}{T_g} \approx 2 \sqrt{\left(\frac{\Delta P}{P} \right)^2 + \left(\frac{\Delta A_i \tau_i}{\gamma_i} \right)^2 + \left(\frac{\Delta \tau_i}{\gamma_i \tau_i} \right)^2 + \left(\frac{\Delta \sigma_j}{\sigma_j} \right)^2 + \left(\frac{\Delta x_j}{x_j} \right)^2} \quad (\text{A3})$$

369 The contribution of Δx_j is negligible owing to low degree of dissociation. Further, the impact
 370 of ΔA_i and $\Delta \tau_i$ on the uncertainty of T_g is minimum when $\gamma_i \rightarrow 1$. In fact, the contribution
 371 of ΔA_i is negligible and only three terms have a role to play on the uncertainty i.e. P , τ_i
 372 and σ_j .

-
- 373 [1] N. M. Laurendeau, Progress in Energy and Combustion Science **14**, 147 (1988).
 374 [2] S. Roy, J. R. Gord, and A. K. Patnaik, Progress in Energy and Combustion Science **36**, 280
 375 (2010).
 376 [3] P. J. Bruggeman, N. Sadeghi, D. C. Schram, and V. Linss, Plasma Sources Science and
 377 Technology **23**, 023001 (2014).
 378 [4] J. Luque, W. Juchmann, and J. Jeffries, Applied optics **36**, 3261 (1997).
 379 [5] A. Lo, G. Cléon, P. Vervisch, and A. Cessou, Applied Physics B **107**, 229 (2012).
 380 [6] K. Gazeli, G. Lombardi, X. Aubert, C. Y. Duluard, S. Prasanna, and K. Hassouni, plasma
 381 **4**, 145 (2021).
 382 [7] S. Zhang, A. Van Gessel, S. Van Grootel, and P. Bruggeman, Plasma Sources Science and
 383 Technology **23**, 025012 (2014).
 384 [8] C. Y. Duluard, L. Invernizzi, K. Hassouni, G. Lombardi, K. Gazeli, and S. Prasanna, Plasma
 385 Sources Science and Technology **33**, 015003 (2023).

This is the author's peer reviewed, accepted manuscript. However, the online version of record will be different from this version once it has been copyedited and typeset.

PLEASE CITE THIS ARTICLE AS DOI: 10.1063/5.0189326

- 386 [9] J.-P. Booth, D. Marinov, M. Foucher, O. Guaitella, D. Bresteau, L. Cabaret, and C. Drag,
387 *Journal of Instrumentation* **10**, C11003 (2015).
- 388 [10] E. Bisceglia, S. Prasanna, K. Gazeli, X. Aubert, C. Y. Duluard, G. Lombardi, and K. Has-
389 souni, *Plasma Sources Sci. Technol.* **30**, 095001 (2021).
- 390 [11] Z. Jia, Y. Fermi, A. Siby, O. Brinza, K. Hassouni, and S. Prasanna, *Plasma Processes and*
391 *Polymers* **20**, 2200180 (2023).
- 392 [12] L. Invernizzi, C. Y. Duluard, H. Höft, K. Hassouni, G. Lombardi, K. Gazeli, and S. Prasanna,
393 *Measurement Science and Technology* **34**, 095203 (2023).
- 394 [13] D. Stefan, A. Siby, Y. Agha, S. Forget, S. Chénais, C. Y. Duluard, L. Invernizzi, H. Höft,
395 S. Prasanna, K. Gazeli, *et al.*, in *AIAA SCITECH 2024 Forum* (2024) p. 0806.
- 396 [14] S. Schröter, J. Bredin, A. R. Gibson, A. West, J. P. Dedrick, E. Wagenaars, K. Niemi, T. Gans,
397 and D. O'Connell, *Plasma Sources Science and Technology* **29**, 105001 (2020).
- 398 [15] A. Gicquel, M. Chenevier, K. Hassouni, A. Tserepi, and M. Dubus, *Journal of applied physics*
399 **83**, 7504 (1998).
- 400 [16] K. Hassouni, A. Gicquel, M. Capitelli, and J. Loureiro, *Plasma Sources Sci. Technol.* **8**, 494
401 (1999).
- 402 [17] Z. Qing, D. K. Otorbaev, G. J. H. Brussaard, M. C. M. van de Sanden, and D. C. Schram,
403 *Journal of Applied Physics* **80**, 1312 (1996).
- 404 [18] A. Gicquel, K. Hassouni, Y. Breton, M. Chenevier, and J. C. Cubertafon, *Diamond and*
405 *Related Materials* **5**, 366 (1996).
- 406 [19] R. K. Garg, T. N. Anderson, R. P. Lucht, T. S. Fisher, and J. P. Gore, *Journal of Physics*
407 *D: Applied Physics* **41**, 095206 (2008).
- 408 [20] M. M. Vasiljević, G. L. Majstorović, D. Spasojević, and N. Konjević, *European Physical*
409 *Journal D* **75**, 112 (2021), aDS Bibcode: 2021EPJD...75..112V.
- 410 [21] H. N. Chu, E. A. Den Hartog, A. R. Lefkow, J. Jacobs, L. W. Anderson, M. G. Lagally, and
411 J. E. Lawler, *Physical Review A* **44**, 3796 (1991).
- 412 [22] A. N. Goyette, W. B. Jameson, L. W. Anderson, and J. E. Lawler, *Journal of Physics D:*
413 *Applied Physics* **29**, 1197 (1996).
- 414 [23] X. Duten, A. Rousseau, A. Gicquel, K. Hassouni, and P. Leprince, *Journal of physics D:*
415 *applied physics* **35**, 1939 (2002).
- 416 [24] W. Wiese and J. Fuhr, *Journal of physical and chemical reference data* **38**, 565 (2009).

This is the author's peer reviewed, accepted manuscript. However, the online version of record will be different from this version once it has been copyedited and typeset.

PLEASE CITE THIS ARTICLE AS DOI: 10.1063/5.0189326

- 417 [25] F. Brouillard and X. Urbain, *Physica Scripta* **2002**, 86.
- 418 [26] U. Meler, K. Kohse-Höinghaus, and T. Just, *Chemical physics letters* **126**, 567 (1986).
- 419 [27] J. Bittner, K. Kohse-Höinghaus, U. Meier, and T. Just, *Chemical Physics Letters* **143**, 571
- 420 (1988).
- 421 [28] A. Catherinot, B. Dubreuil, and M. Gand, *Physical Review A* **18**, 1097 (1978).

This is the author's peer reviewed, accepted manuscript. However, the online version of record will be different from this version once it has been copyedited and typeset.
 PLEASE CITE THIS ARTICLE AS DOI: 10.1063/5.0189326

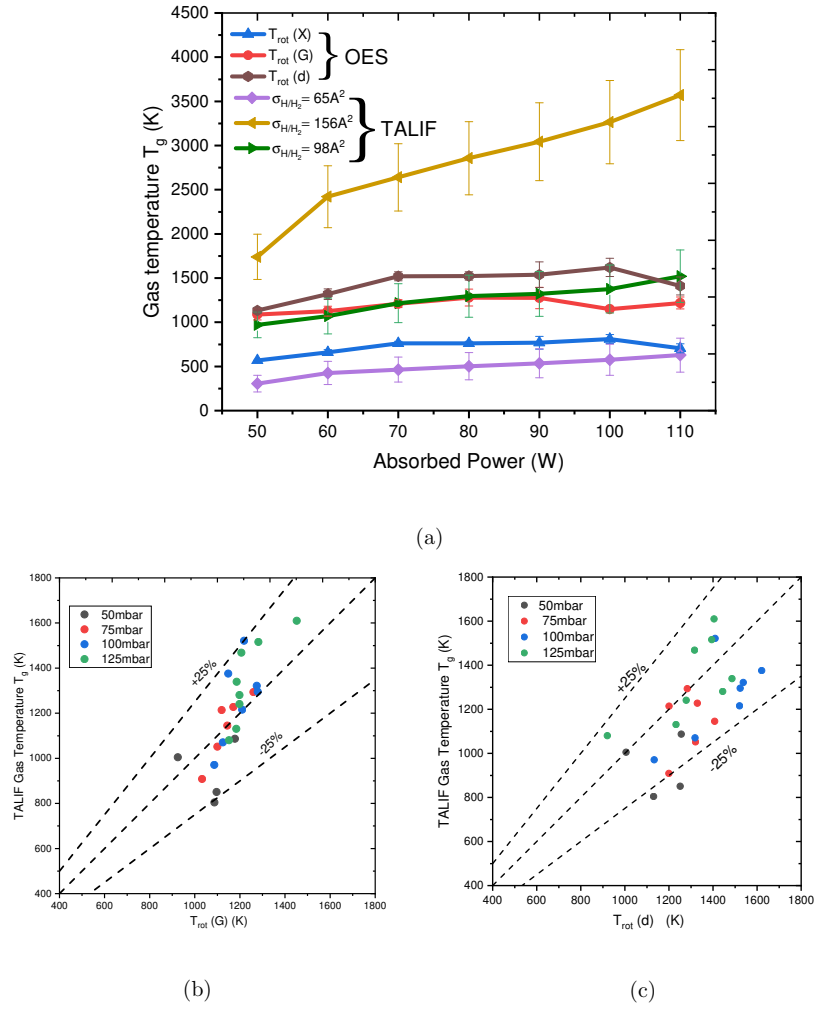


FIG. 7. (a) Comparison of gas temperatures measured using OES and ps-TALIF at 100 mbar and parity plot comparing gas temperature measurement from ps-TALIF using $\sigma_{H/H_2} = 98 A^2$ with rotational temperatures (b) $T_{rot}(G)$ and (c) $T_{rot}(d)$.

This is the author's peer reviewed, accepted manuscript. However, the online version of record will be different from this version once it has been copyedited and typeset.

PLEASE CITE THIS ARTICLE AS DOI: 10.1063/5.0189326

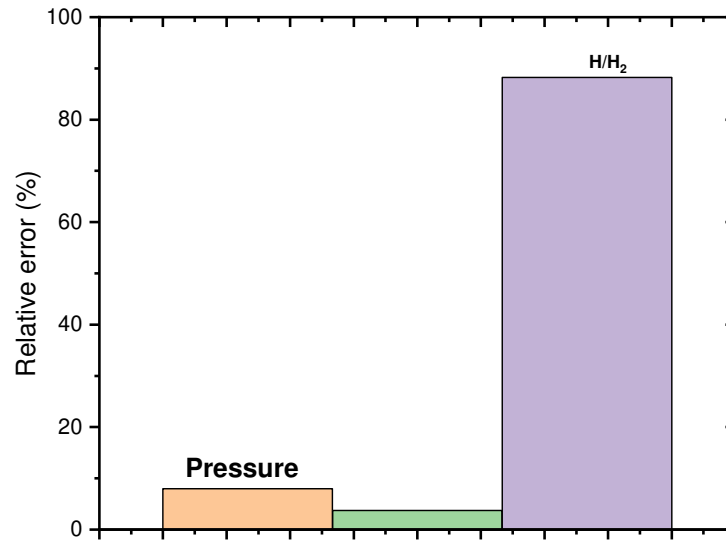


FIG. 8. Relative errors for the different terms of the gas temperature equation at 100 mbar and 100W.

This is the author's peer reviewed, accepted manuscript. However, the online version of record will be different from this version once it has been copyedited and typeset.

PLEASE CITE THIS ARTICLE AS DOI: 10.1063/5.0189326

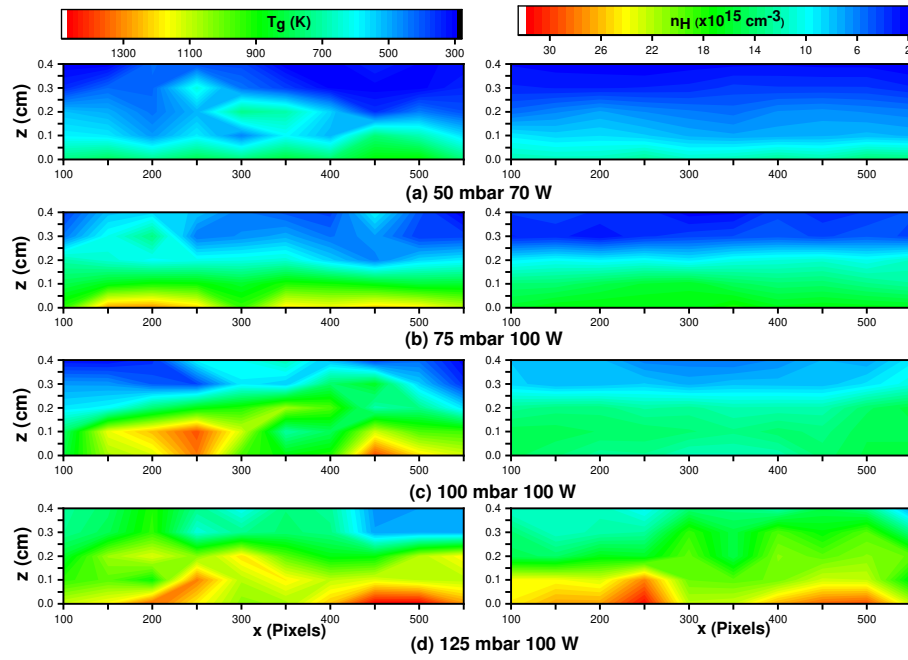


FIG. 9. Constructed 2D contour plots of H-atom density and T_g for different pressures. The x-axis is referred to in pixels as axial calibration (i.e. along x-axis) was not performed. y-axis refers to z with 0 referring to the first possible laser measurement which is about 0.5 mm from the base of the torch.